Journal of Computational and Applied Research in Mechanical Engineering
jcarme.sru.ac.ir
SRTTU
JCARME
ISSN: 2228-7922

Research Paper

Numerical prediction of the drag coefficient of bluff bodies in three-dimensional pipe flow

A. Tamil Chandran[a*], T. Suthakar[b], K. R. Balasubramanian[b], S. Rammohan[a] and Jacob Chandapillai[a]

[a]*Fluid Control Research Institute, Palakkad, Kerala- 678623, India*
[b]*Mechanical Engineering department, National Institute of Technology- Trichirapallai, Tamil Nadu, India*

Article info:

Article history:

Received: 13/07/2020
Revised: 28/10/2021
Accepted: 01/11/2021
Online: 03/11/2021

Keywords:

Drag coefficient,
Pressure coefficient,
Turbulence model,
Computational fluid dynamics,
Bluff body,
Friction coefficient.

[*]Corresponding author:
tamilchandran@fcriindia.com

Abstract

Numerical analysis of drag coefficient of three-dimensional bluff bodies such as flat plates, cylinder, triangular prism, semicircular profiles located in the flow path of the pipe was performed. Bluff bodies of various lengths are analysed using a turbulence model. The effect of bluff body thickness on drag coefficient was analysed. A significant observation of the study is the reduction in drag coefficient with an increase in thickness. Effect of pressure coefficient on drag coefficient was evaluated. The study confirms that frictional coefficient has negligible effect on drag coefficient in the studied Reynolds number range. Change in drag coefficient over a wide range of Reynolds number was studied and is reported. Irrespective of geometry and length, the study indicates that there is a significant difference in drag coefficient between two dimensional and three dimensional simulation studies. It is also concluded that the length of a bluff body in a confined domain has a significant effect on its drag coefficient.

1. Introduction

An understanding of drag coefficient of bluff bodies is vital to engineering design in many applications, including aerodynamic loading on structures, drag reduction in automobiles, etc., [1]. Studies on flow past cylinders and plates are classical problems in fluid mechanics considering the range of engineering applications. Available data are mostly for high Reynolds number regions. Drag force acting on bluff body is mainly due to a combination of frictional drag and pressure drag.

Friction drag is created by wall shear stress acting on the body. The friction drag acting on

the flat plates having a frontal area 'A', oriented parallel to upstream flow is given by Eq. (1), [2]

$$D_{ff} = C_{df} \frac{1}{2} \rho v^2 A \quad (1)$$

On the other hand, pressure drag, also known as form drag, is directly proportional to the pressure force on an object and also strongly depends on shape or form of the object. Pressure drag is a function of magnitude and orientation of the surface element on which pressure force acts and is given by Eq. (2) [2].

$$D_{pf} = C_{dp} \frac{1}{2} \rho A v^2 \quad (2)$$

To determine drag coefficient for various shapes, numerous experimental and numerical studies were conducted on various shapes; and it has been well documented [3].

Norberg [4] has reviewed the lift force acting on cylinders in cross flow, with experimental assessment of dynamic pressure variation around the bluff body. This is the source of pressure drag. Gu [5] describes the flow around cylinders with splitter plates. In his study, pressure on the cylinder was measured for the length to diameter ratio up to 6.0 in the Reynolds number range from $3x10^4$ to $6x10^4$. Bo Zhou [6, 7] reports the drag and lift coefficients for cylinders at various surface conditions by both experiment and numerical analysis.

Castro [8] reports on blockage effect, with flat plates over the Reynolds number range of $2.5x10^4$ to $9.0x10^4$. Lisoski [9] used towing tank method to determine the drag force effect on a flat plate. Rostane [10] discusses the effect of a hole on a bluff body on its drag coefficient as brought out by CFD analysis. Khalkhali [11] numerically analysed drag and lift coefficient of aero foil using evolutionary optimization technique.

Numerous theoretical studies for a flat plate and circular cylinders are reported for two-dimensional (2-D) analysis, where the drag forces were not comparable to experimental results. These 2-D analyses overpredicted the drag forces by a factor up to 1.6 as compared to experimental results. Najjar [12] discussed the drag coefficient for flat plate using both 2-D and 3-D techniques, where the average drag coefficient determined by 3-D analysis was shown closely matching the experimental results of Fage and Johansen [13].

The drag force on a normal flat plate is significantly overestimated in 2-D simulations [13]. The published literature on most 3-D numerical analyses is observed to be in the free field environment; and it was mainly for flat plates and circular cylinders. However, numerous applications require knowledge of drag coefficients of structures of various shapes and bluff bodies located in confined domain.

Fage [13] has conducted experiments on flat plates with various widths and also with various angles of attack of flow to study the velocity distribution behind the test specimen to determine the drag coefficient. Dey [14] has numerically studied the drag of a square cylinder with thorn on the front, back side of it. It was done for the Reynolds number of 100 and 180. Alex [15] has numerically studied the drag force acting on circular cylinder using 2-D analysis by including moving near the wall effect. Karthik [16] has studied a circular cylinder with a splitter plate on the back side of the cylinder by using three dimensional analysis. The splitter used has a width of 0.5d to 3d and it was done at a Reynolds number of 97300. Tian [17] has studied flow over a rectangular plate with various radii of curvature at the end of the plate. Based on the review conducted, it was observed that 3-D drag coefficient studies were conducted on limited shapes and also with fixed length.

This paper discusses flow through a pipe with the bluff body placed perpendicular to flow direction. Bluff bodies of length to pipe diameter ratio 0.1 to 1.0, Reynolds number $1x10^3$ to $6x10^5$ with different cross-sections such as rectangular to square, cylindrical, triangular and semi-circular front in the triangle are evaluated.

The outline of subsequent sections of the paper is as below:

Section 2 describes the problem definition and geometry. Section 3 discusses the mathematical formulation and numerical methods. The computational overview and

convergence studies are presented in Sections 4 and 5 respectively. Results and discussion are in Section 6 and the conclusion is given in Section 7.

2. Problem definition

In this study, the 3-D analysis of four geometric shapes of bluff bodies having various geometrical dimensions is performed using computational fluid dynamic code.
The geometrical shapes of the bluff bodies considered for the study are given in Fig. 1. The ratio between the length of the bluff body and diameter of the pipe, i.e. $\left(\frac{l}{d}\right)$ considered for this analysis is in the range of 0.1 to 1.00.

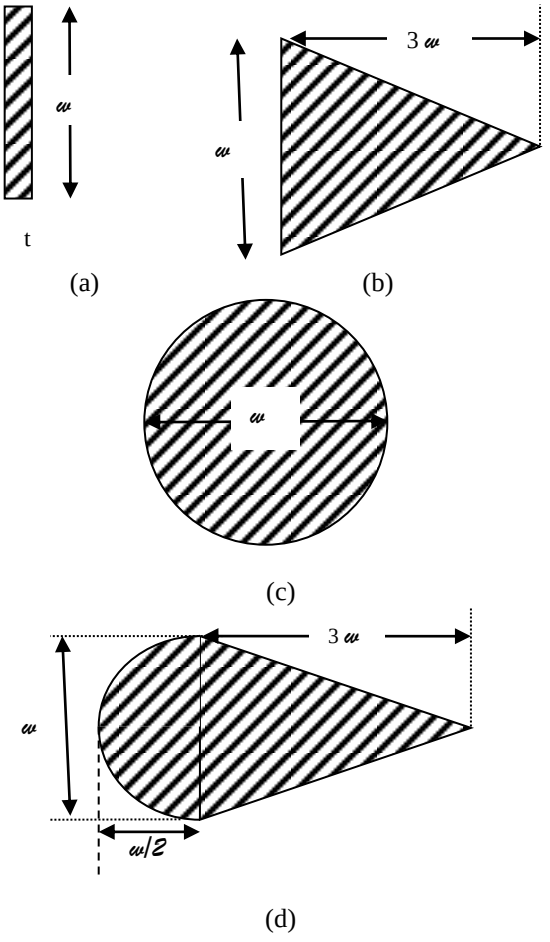

Fig. 1. Geometrical shapes: (a) Plate/ Beam, (b) Triangle (Triangular prism), (c) Circular (cylinder) and (d) Triangle with semicircular front.

In addition to $\left(\frac{l}{d}\right)$ ratio, the thickness effect was studied for the case of the beam. In this case, thickness to width ratio, 't/w' considered is from 0.1 to 1.

3. Mathematical formulation and numerical methods

Turbulence in fluid flow is 3-D in nature and unsteady with a large range of scale motions. As a result of three - dimensionality and unsteadiness, for numerically computing turbulence in the enormous range of scales must be resolved. For simplified steady-state fluid flow cases, it is not necessary to simulate the detailed instantaneous flow. It leads to a great reduction of the computational time. Derivation of governing equation for turbulent flow was done by using continuity and Navier-Stokes equations, by splitting the pressure and velocity terms in to time mean value and corresponding fluctuation. It yields to an additional term that is known as apparent stresses of turbulent flow or Reynolds stresses. Since turbulence is considered as eddying motion, the apparent stresses are caused by eddy viscosity. To numerically solve the equations, various turbulence models were proposed; some of the methods are one equation Spalart- Allmaras model, two equation k-ε models and k-omega model, and seven equations Reynolds stress model. Chakraborthy [18] reviewed various turbulence models and suggested that two equation k-ε models be used for internal fluid flow computation.

3.1. Mathematical formulation

The governing equations for turbulence incompressible fluid flow are as given in Eq. (3)

$$\frac{\partial U_i}{\partial x_i} = 0 \tag{3}$$

The momentum conservation equation, i.e., Navier-stokes Eq. (4)

$$U_j \frac{\partial U_i}{\partial x_j} = -\frac{1}{\rho}\frac{\partial p}{\partial x_i} + \frac{\partial}{\partial x_j}\left(\nu\left(\frac{\partial U_i}{\partial x_j} + \frac{\partial U_j}{\partial x_i}\right) - \overline{u_i' u_j'}\right) \tag{4}$$

where U_i are the components of mean velocity, x_i are the Cartesian coordinates, 'p' is the mean pressure, and u_i' are the fluctuations of the velocity components around their mean values. $-\overline{u_i'u_j'}$ is the Reynolds - stress tensor. To obtain a closed set of equations, the unknown Reynolds stress tensor needs to be modelled. For modelling, Reynolds stress can be decomposed into an isotropic and another in anisotropic part as is given in Eq. (5) .

$$-\overline{u_i'u_j'} = -\frac{2}{3}\delta_{ij}k + \nu_t\left(\frac{\partial U_i}{\partial x_j}+\frac{\partial U_j}{\partial x_i}\right) \quad (5)$$

First part of the RHS side of the equation is the isotropic part and the second term is the anisotropic part. The anisotropic part is also known as Boussinesq eddy viscosity approximation; where ν_t the turbulent kinematic viscosity, 'k' -turbulent kinetic energy and δ_{ij} - Kronecker delta.

Turbulent kinetic energy 'k' is derived from the arithmetic average of the diagonal elements of the stress tensor in Eq. (6).

$$k = \frac{1}{2}\overline{u_i'u_i'} = \frac{1}{2}\left(\overline{u_x'u_x'} + \overline{u_y'u_y'} + \overline{u_z'u_z'}\right) \quad (6)$$

Determination of turbulent kinematic viscosity can be achieved by solving auxiliary field equations and is dependent on the used turbulence model.

To numerically solve the equations, various turbulence models are available. Two equation k-ε models are widely used for incompressible internal fluid flow computation. The k-ε model is further classified into standard k-ε model, RNG k-ε model, and Realizable k-ε model. From the solver independence studies conducted and as reported in section 5, standard k-ε model is used for this study and its formulation is as discussed below.

3.2. Standard k-ε model

Harlow [19] has first developed the standard k-ε turbulence model and it was extensively tested for suitability for turbulence modelling by Launder and Spalding [2]. The transport equations of 'k' and 'ε ' are presented in Eqs. (7-10).

$$\frac{\partial k}{\partial t} + U_j\frac{\partial k}{\partial x_j} = \frac{\partial}{\partial x_j}\left[\left(\nu + \frac{\nu_t}{\sigma_k}\right)\frac{\partial k}{\partial x_j}\right] + G - \varepsilon \quad (7)$$

$$\frac{\partial \varepsilon}{\partial t} + U_j\frac{\partial \varepsilon}{\partial x_j} = \frac{\partial}{\partial x_j}\left[\left(\nu + \frac{\nu_t}{\sigma_\varepsilon}\right)\frac{\partial \varepsilon}{\partial x_j}\right] + C_{\varepsilon 1}\frac{\varepsilon}{k}G - C_{\varepsilon 2}\frac{\varepsilon^2}{k} \quad (8)$$

$$G = -\overline{u_i'u_j'}\frac{\partial U_i}{\partial x_j} = \nu_t\left(\frac{\partial U_i}{\partial x_j} + \frac{\partial U_j}{\partial x_i}\right)\frac{\partial U_i}{\partial x_j} \quad (9)$$

Turbulence kinematic viscosity is

$$\nu_t = C_\mu\frac{k^2}{\varepsilon} \quad (10)$$

Launder et al. [20] has made an extensive examination of free turbulent flows to derive the constants appearing in Eqs. (7-9), and the values are given in Table 1.

Based on the survey conducted, it is observed that k-ε model is good enough for most cases. It has some known deficiencies such as not predicting the kinetic energy correctly at recirculation regions that is due to epsilon in the equation.

3.3. Numerical methods

Finite volume method has become the most popular method for turbulence studies. In numerical analysis, proper selection of discretization and type of mesh algorithm used play a major role in solution accuracy, computational efficiency and convergence of the solution. Since the entire fluid domain was modelled as a single part, for meshing, the assembly meshing method was used. For assembly meshing, ANSYS has two different meshing algorithms including CutCell and Tetrahedrons. CutCell is a Patch Independent Mesher, and it is very well suitable for moderately clean CAD models. It results in a mesh of up to 95% hex cells, which leads to accurate solutions [21]. In this study, computational fluid dynamic (CFD) module of ANSYS software was used with the following settings [22].

Table 1. Values of constants in standard k-ε turbulence model.

C_μ	$C_{\varepsilon 1}$	$C_{\varepsilon 2}$	σ_k	σ_ε
0.09	1.44	1.92	1.0	1.3

Model: Viscous pressure based k-ε turbulent model with standard wall function,
Scheme: pressure velocity coupling PISO with skewness correction and Neighbor correction
Spatial discretization:
Gradient: Least square cell based, Pressure: Second order,
Momentum: Second order upwind
Turbulent Kinetic energy: Second order upwind,
Turbulent Dissipation rate: Second order upwind with convergence criteria for continuity, X- is velocity, Y- is velocity, Z – is velocity, k and ε are greater than 0.001.

4. Computational overview

The computational domain used for doing this analysis consists of a pipe having a diameter of 'd' and upstream and downstream distances are decided based on the optimization studies carried out by researchers. Najjar [23] and Vagesh [24] considered the upstream distance of 5W and a downstream distance of 20W with a flat plate in the cross flow. Tian [17] has studied and optimized the upstream and downstream distance for the domain with a flat plate. Upstream and downstream distance optimized by Tian [17] for dynamic analysis is 7.5W and 20W. In the present study, upstream and downstream distances are optimized by performing a domain independence study. From the studies conducted, upstream boundary was located at 5W from the front side and the downstream boundary was located at 20W from the back side of the bluff body.

The computational domain with boundary condition is as shown in Fig. 2. At the inlet boundary, a uniform flow having velocity in one direction (flow direction), and other two directions was considered as zero velocity. The pressure and velocities were set to zero at the walls. Due to geometrical symmetry, only half of the domain was used for analysis by defining a symmetry boundary at the symmetry plane.
The computational domain was meshed with the auto mesh option available in ANSYS with all elements being as cut mesh. At bluff body walls, a special layer was considered and meshed accordingly.
The distance of the first layer node away from the bluff body surface was based on the calculation as below, with the wall adjustment grid height 'y$^+$' being less than 20 [17].
Wall adjacement grid height y^+ is as in Eq. (11).

$$y^+ = \frac{\rho U_T \Delta y_1}{\mu} \tag{11}$$

where μ -viscosity, U_T - frictional velocity in Eq. (12) and Δy_1 - first cell height

$$U_T = \sqrt{\frac{\tau_w}{\rho}} \tag{12}$$

The wall shear stress τ_w in Eq. (13) can be calculated from the skin friction coefficient, C_f . For external flow, empirical estimate of $C_f = 0.058\, Re^{-0.2}$

$$\tau_w = \frac{1}{2} C_f \rho U^2 \tag{13}$$

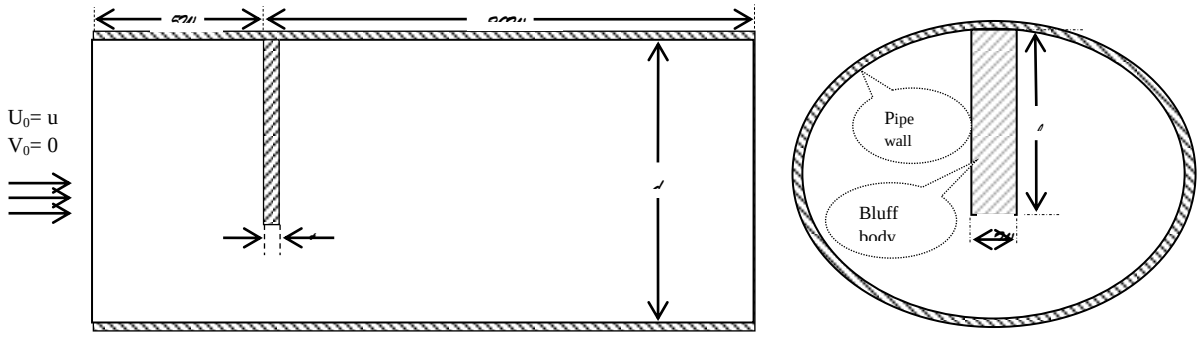

(a) (b)

Fig. 2. Computational domain: (a) Front view and (b) Side view.

5 Convergence studies

Convergence studies were carried out to optimize the length of the flow domain and mesh size. Results of all the cases/conditions conducted as part of convergence studies are as given in Table 2(a and b). The drag coefficient (C_d) is considered for convergence studies. The C_d is defined as in Eq. (14)

$$C_d = \frac{F_z}{\frac{1}{2}U^2 A} \quad (14)$$

where F_z is the force acting on the bluff body in the flow direction which is calculated directly by integrating the pressure and shear stress along the surface; where '**A**' is the reference frontal area and 'U' is the free stream velocity. Convergence studies were conducted for the $\left(\frac{l}{d}\right) ratio\ of$ 0.39.

5.1. Domain independence study

In CFD analysis, the sizes of the flow domain and wall boundaries play a major role in its results. In the present study, since the bluff body is kept in a pipe, the length of the domain needs to be optimized for the analysis. Hence, the length of the flow domain was varied by keeping the same mesh size for all cases. Results of domain independence study conducted are reported for cases 1 to 5 in Table 2(a).

Table 2(a). Domain independence study.

Case	Length of flow domain	Elements / unit volume	Drag coefficient C_d
1	10 W	197	1.609
2	15 W	169	1.736
3	20 W	152	1.781
4	25 W	125	1.801
5	30 W	119	1.802

Table 2(b). Grid independence study.

Case	Length of flow domain	Elements / unit volume	Drag coefficient C_d
6	25W	70	1.829
7	25W	78	1.814
8	25 W	92	1.808
9	25 W	125	1.801
10	25 W	273	1.802

From the studies conducted, it is observed that the results of cases 1 and 2 have deviation of more than 5 % with the results of case 3 to 5. In cases 4 and 5 that are not significantly different, the relative changes are within 1% and it is the in line with the deviation reported by Tian [17]. Based on the convergence studies conducted, and the results reported by the researchers, the flow domain length of 25W is used for further analysis.

5.2. Grid independence study

Grid independence studies were conducted for the optimized domain size of 25W with various grid sizes. This is given in Cases 6 to 10 in Table 2(b). For this study, the element density of the fluid domain was increased gradually that is reported. From cases 6 and 7, it is observed that the deviation in drag coefficient is more than 1%. By further increasing the grid density, the deviation between cases was reduced to less than 1%. From the convergence results, mesh density of 125 per unit volume is used for further analysis.

5.3. Solver independence study

For turbulence studies various solvers are developed and put into use. Based on the reviews conducted, it is observed that, k-ε turbulence model solver is one of the frequently used solvers for incompressible fluid flow analysis. Within k-ε turbulence model, the solver independence study was conducted between standards, RNG and Realizable k-ε turbulence models. The outcome of the study is reported in Table 3. Results from these models indicate a variation of 1%. So for further analysis, standard k-ε solver was used.

Table 3. Solver independence study results.

Case	Solver type	Length of flow domain	Elements / unit volume	C_d
11	Standard k-ε	25 W	125	1.801
12	RNG k-ε	25W	125	1.800
13	Realizable k-ε	25 W	125	1.802

6. Results and discussion

Drag coefficient analysis was done on four different geometries of bluff bodies. Its $\left(\frac{l}{d}\right)$ ratio is from 0.10 to 1.00 and is as in Fig. 1. Initially, it was done at a reference Reynolds number of 1.1×10^4 and further extended the studies in the range of 1.0×10^3 to 6.0×10^5. Reynolds number was calculated based on the width 'w' of the bluff body. To study the thickness effect, the analysis was further carried out by varying its thickness for the thickness to width ratio $\left(\frac{t}{w}\right)$of 0.1 to 1.0. It was done only for the beam. The initial part of the analysis was to optimize the length of the flow domain, mesh density and solver selection; as specified in Tables 2 and 3 in section 5. Further, it was analysed for drag coefficient, pressure coefficient, frictional forces and velocity distribution.

6.1. Drag coefficient

Drag coefficient (C_d) is a geometrical constant which depends upon the geometry and orientation. It is used to estimate the forces acting on the bluff body due to fluid flow. Drag forces can be directly measured in the $1.1x10^3$ and it is 1.801. determined for a flat plate having 'l/d' ratio of Further, it was analysed for other 'l/d' ratios and found that the 'C_d' is varying from 1.6 to 1.92; which is very close with the experimental results of 1.85 [19], 1.88 [25] and 1.84 [9] reported experimental studies by using force measuring setups and the 'C_d' can be determined. In numerical analysis 'C_d' can be estimated from the obtained pressure and shear forces acting on the body. In this study, initially 'C_d' was 0.39, at a reference Reynolds number of Similarly, the analysis for other geometries such as Cylinder, Triangle, and Triangle with semicircular front was also carried out and the 'C_d' values varied from 0.739 to 0.845, 1.58 to 1.832 and 0.459 to 0.603 respectively. Details are reported in Table 4. From the results it is observed that the pipe wall boundary significantly influenced in the 'C_d' value. The effect is significant, when the 'l/d' ratio is less than 0.2 and when it is 1.00. From the geometrical shapes analysed, the maximum 'C_d' value was observed at the 'l/d' ratio of 0.84.

To determine the effect of Reynolds number in 'C_d', further it was analysed for the Reynolds number range of 1×10^3 to 6×10^5, with 'l/d' ratio from 0.2 to 1.00, as is reported in Table 5. Averaged 'C_d' over the range of Reynolds number and 'l/d' ratio for the plate, Triangle, Cylinder and Triangle with semicircular front is 1.71, 1.73, 0.94 and 0.50, respectively.

Table 4. Drag coefficient at Reynolds number of 1.1×10^3.

l/d ratio	Geometrical shape			
	Beam/ Plate	Cylinder	Triangle	Triangle with semicircular front
0.10	1.49	0.79	1.55	0.543
0.20	1.607	0.806	1.576	0.553
0.39	1.801	0.831	1.702	0.562
0.55	1.895	0.838	1.764	0.552
0.71	1.901	0.842	1.801	0.567
0.84	1.92	0.845	1.832	0.603
1.00	1.826	0.739	1.695	0.459

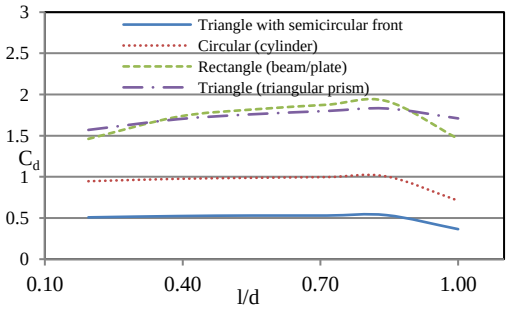

Fig. 3. Drag coefficient (Reynolds number 1×10^3 to 6×10^5).

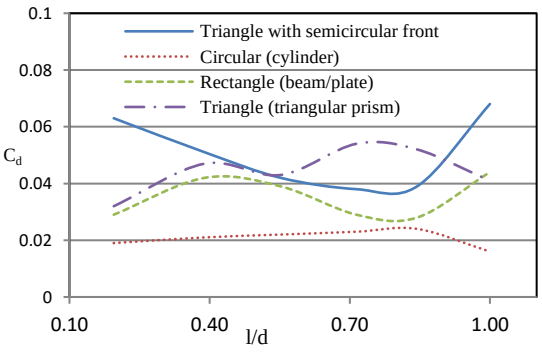

Fig. 4. Standard deviation in drag coefficient (Reynolds number 1×10^3 to 6×10^5).

Table 5. Drag coefficient (Reynolds number 1×10^3 to 6×10^5).

Geometrical shape	Drag coefficient		
	Maximum	Minimum	Average
Beam/Plate	1.92	1.46	1.71
Cylinder	1.01	0.71	0.94
Triangle	1.83	1.57	1.73
Triangle with semicircular front	0.61	0.36	0.50

Due to a similarity in frontal shape, drag coefficients of both the plate and triangle are close. Maximum and minimum values observed for the cylinder is from 1.01 to 0.71 with an average value of 0.94 and is comparable to the experimental result of 1.07 reported by Zhou [7].

Triangle with semicircular front end is having 'C_d' from 0.36 to 0.61 over the range of Reynolds number and 'l/d' ratio. For the study conducted, triangle with semicircular front end has lesser 'C_d' compared to the other shapes. Plots of 'C_d' averaged over the Reynolds number for 'l/d' ratio are shown in Fig. 3. Standard deviation in 'C_d' averaging is in Fig. 4.

Further, the effect of plate thickness on 'C_d' value was studied for width to thickness ratio 'w/t'. It was done up to the ratio of 1.00 as reported in Table 6. The 'C_d' value averaged over Reynolds number and 'l/d' ratio for beams having various 'w/t' ratios from 1.71 to 1.61. Maximum value of 1.92 is observed for the 'w/t' ratio of 0.1 and 1.76 for the 'w/t' ratio of 1.0. Determined 'C_d' of 1.76 for the square section is in line with the result of 1.75 reported by Dey [14].

When the ratio varies from 0.1 to 1.0, reduction in 'C_d' value is observed and it is up to 6%. Plots of 'C_d' averaged over the Reynolds number for l/d ratio and its standard deviation in averaging are shown in Fig. 5.

6.2. Pressure coefficient

Pressure coefficient is the ratio between the pressure difference and dynamic pressure in the flow loop and it can be written as $C_p = \frac{2(P-P\infty)}{\rho\, U_\infty{}^2}$. It is the source for pressure drag. Pressure distribution contour for a sample case, having beam as a bluff body at a reference Reynolds number is as shown in Fig. 6. From the pressure contour, maximum pressure difference of 1100 Pascal is observed and it is between front and rear side of the beam. Just behind the bluff body, it is observed that the static pressure is always less than the free stream static pressure and it leads to the negative pressure coefficient, just behind the bluff body.

Table 6. Drag coefficient with 'w/t' ratio (Reynolds number $1x10^3$ to $6x10^5$).

Beam 'w/t' ratio	Drag co efficient		
	Maximum	Minimum	Average
0.10	1.92	1.46	1.71
0.20	1.87	1.45	1.70
0.40	1.90	1.45	1.68
0.60	1.84	1.40	1.66
0.80	1.82	1.39	1.64
1.00	1.76	1.32	1.61

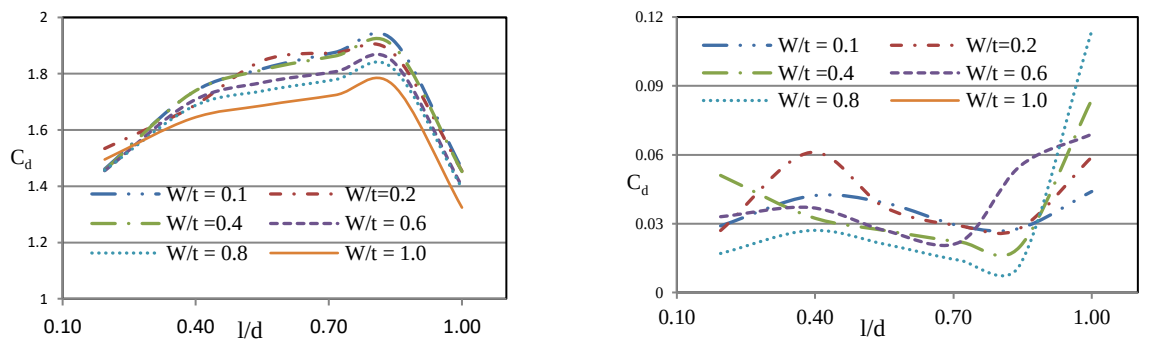

(a) (b)

Fig. 5. Drag of Beam in Reynolds number range of 1×10^3 to 6×10^5: (a) drag co efficient and (b) standard deviation.

Moving further downstream of the bluff body, the pressure got recovered and pressure coefficient is reaching to a positive value. Toward the tip of the beam, maximum negative pressure was observed in the back side wall and it leads to the maximum pressure coefficient, just behind the bluff body at the tip. Pressure coefficient on the wall can be directly plotted from the wall boundaries and for plotting the results in axial and radial directions of the flow, Line/rack are considered and given in Fig. 7.

Pressure coefficient at the front and rear walls of the bluff body were plotted and reported. In both beam and triangle, due to the similarity in the shape of the front wall, similar pattern and nearest values of 'C_p' with maximum of 1.4 are observed. Its plots are as given in Fig. 8. (a) and (b) respectively. When the ratio of 'y/l' is near one, the 'C_p' gets reduced and reaches zero. At the back wall, 'C_p' value is between -0.5 to -0.7 for beam, and for triangle it is from 0 to -1. Due to similarity in 'C_p' of the front wall, for both the cases 'C_d' values are close to each other.

In the case of a triangle with semicircular front and cylinder, 'C_p' value plots of front wall have similar patterns with an average value of -0.8 and 0.4 respectively. Its plots are as given in Fig. 8. (c)and (d) respectively. For both cases, rear walls have negative 'C_p' values and averaged values are -1.0 and - 0.6 respectively.

Due to the reduced 'C_p', in the case of triangle with semi-circular front, 'C_d' value is also comparatively lesser than the case of the cylinder.

Pressure coefficient in the flow domain, in the flow direction of 'z' with various 'y/l' ratios and 'x' coordinates at zero are plotted. Due to the presences of bluff body in the flow path, a discontinuity in 'C_p' is observed for the 'y/l' ratio of less than 1. When 'y/l' is 1 or higher, the effect of bluff body is Minimized; but till the disturbance in the flow path is observed and is represented in the form of 'C_p' in the plots. The 'C_p' of beam and triangle is as given in Fig. 9. (a) and (b) respectively. The 'C_p' of other two geometries as given in Fig. 9.(c) for 'triangle with semicircular front' and in Fig. 9.(d) for 'cylinder'.

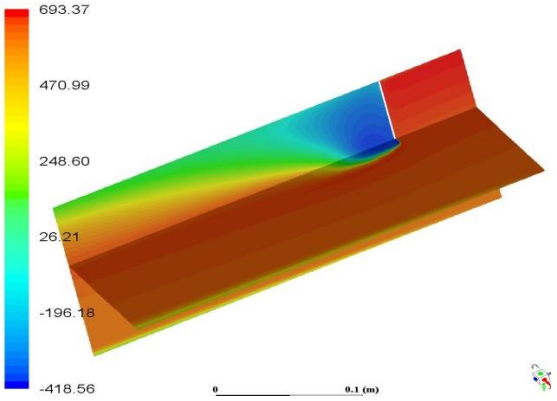

Fig. 6. Pressure distribution contour.

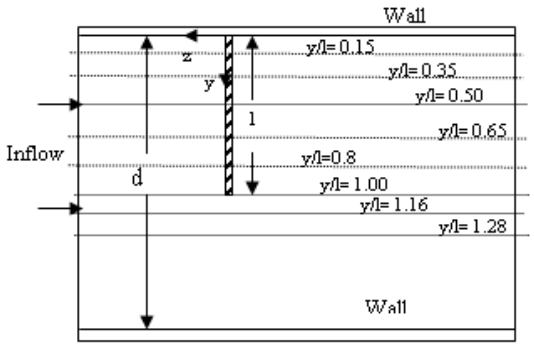

Not to scale (a)

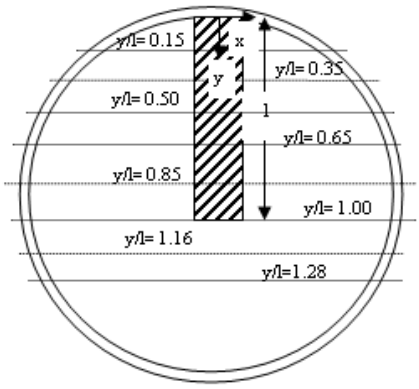

Not to scale (b)

Fig. 7. Coordinate details for result representation: (a) Sectional view (front) and (b) Side view.

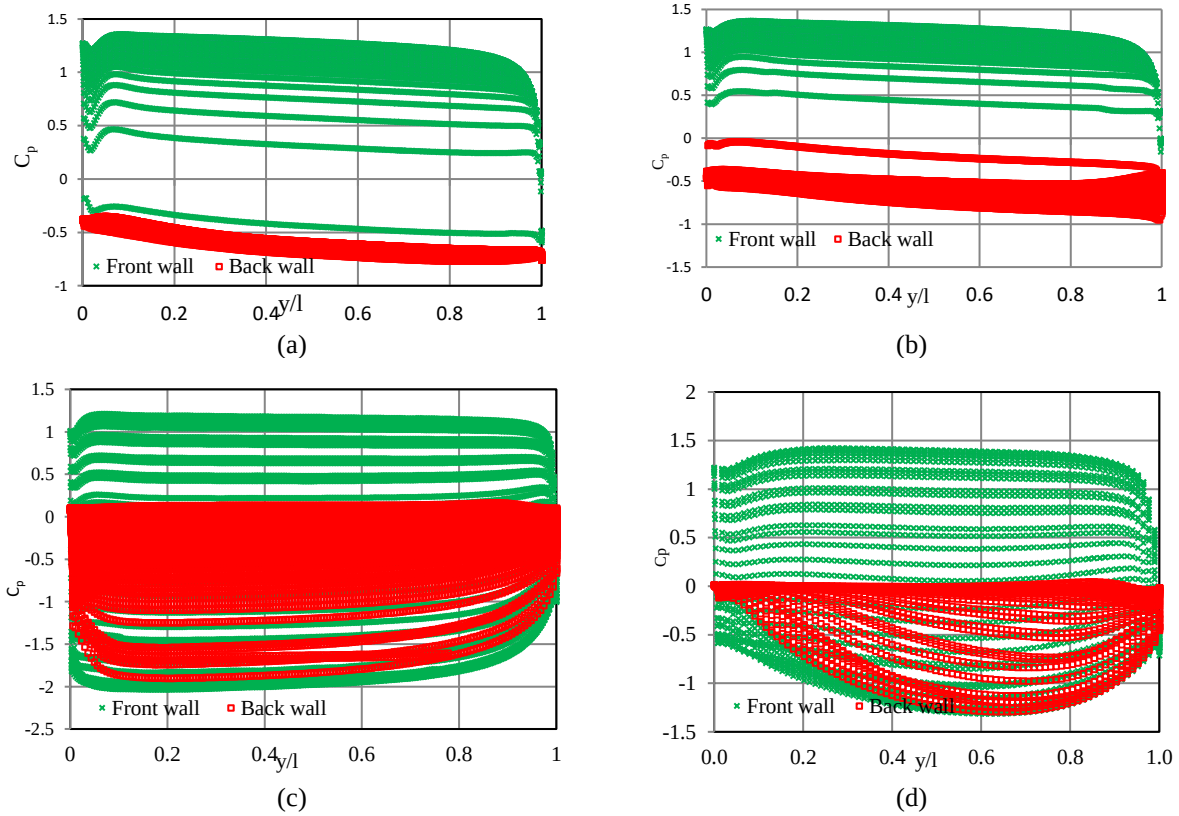

Fig. 8. Wall pressure coefficient: (a) Beam, (b) triangle, (c) Triangle with semicircular front, and (d) cylinder

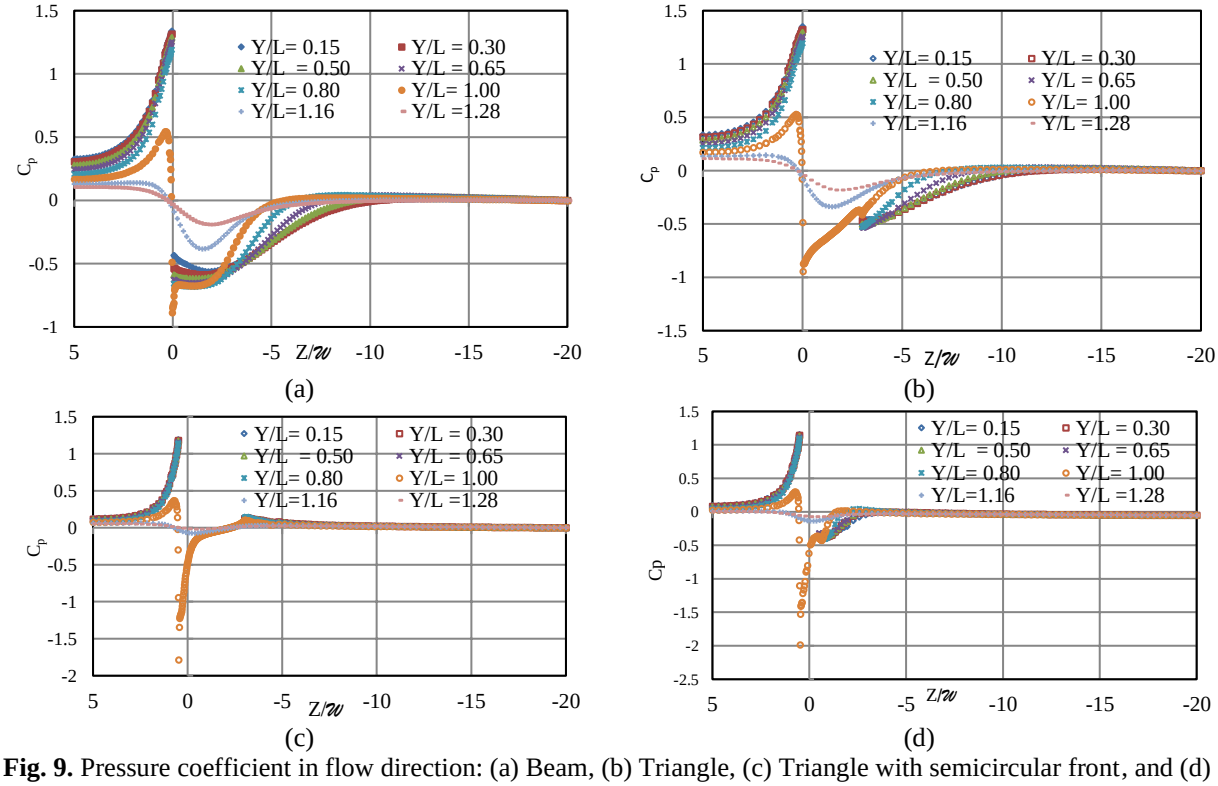

Fig. 9. Pressure coefficient in flow direction: (a) Beam, (b) Triangle, (c) Triangle with semicircular front, and (d) cylinder.

In all the cases, downstream side flow is fully developed within the 'Z/W' ratio of 10 and it is the evident that the 'Z/W' ratio of 20 used for the downstream side is justifiable.

Both in beam and triangle, similar patterns of 'C_p' are observed and the effect of flow disturbance in the down downstream side due to the triangular pattern is negligible. Similarly, the cylinder and semi-circular front with triangle have a similar pattern. In this case, flow has been fully developed within the 'z/w' ratio of 4.

As indicated in Fig. 7., pressure coefficient in the direction of 'x' with various 'y/l' ratios is plotted and is as given in Fig. 10. It is found that in all cases, near the pipe wall, pressure coefficient is zero. In the case of the beam, when 'y/l' is less than or equal to 1, pressure near the sidewall of the beam is less than that of the line pressure; it leads to the negative 'C_p' near, right and left side of the wall. Due to geometrical similarity, both sides of the walls have a similar value of 'C_p'. Maximum 'C_p' value of -0.9 was observed near the wall of the beam. When moving further down from tip of the bluff body, the pressure gets stabilized and reaches the line pressure and it leads the 'C_p' to zero. When 'y/l' is more than 1, the pressure near the beam has got disturbed and got reduced slightly and it gives a 'C_p' value of -0.07. As in beam, a similar trend in 'C_p' was observed on both cylinder and triangle with semicircular front, except its amplitude. The maximum 'C_p' value observed in the cylinder is -2.0 and for the semicircular front coupled with triangles it is -1.5. In the case of the triangle, the pressure has been developed near the side walls and it leads to positive 'C_p'.

6.3. Friction forces

When a body is placed in a fluid flow, it will be subjected to various forces due to fluid flow. Such forces acting on the body, in the flow direction is the combination of drag force and frictional force. The frictional force acting on the bluff body and its frictional coefficient are discussed in this section. The frictional force is $= C_{df}\frac{1}{2}\rho v^2 A$; where 'C_{df}' is a frictional drag coefficient. It can be determined by CFD by using the ratio between the shear forces acting on the wall and dynamic pressure and frontal area of the body. Plots of frictional coefficient in front and back side of the walls are as given in Fig. 11. In all cases, the friction coefficient of the front wall is comparatively higher than the back wall; it is because of the negligible amount of shear force acting on the back wall.

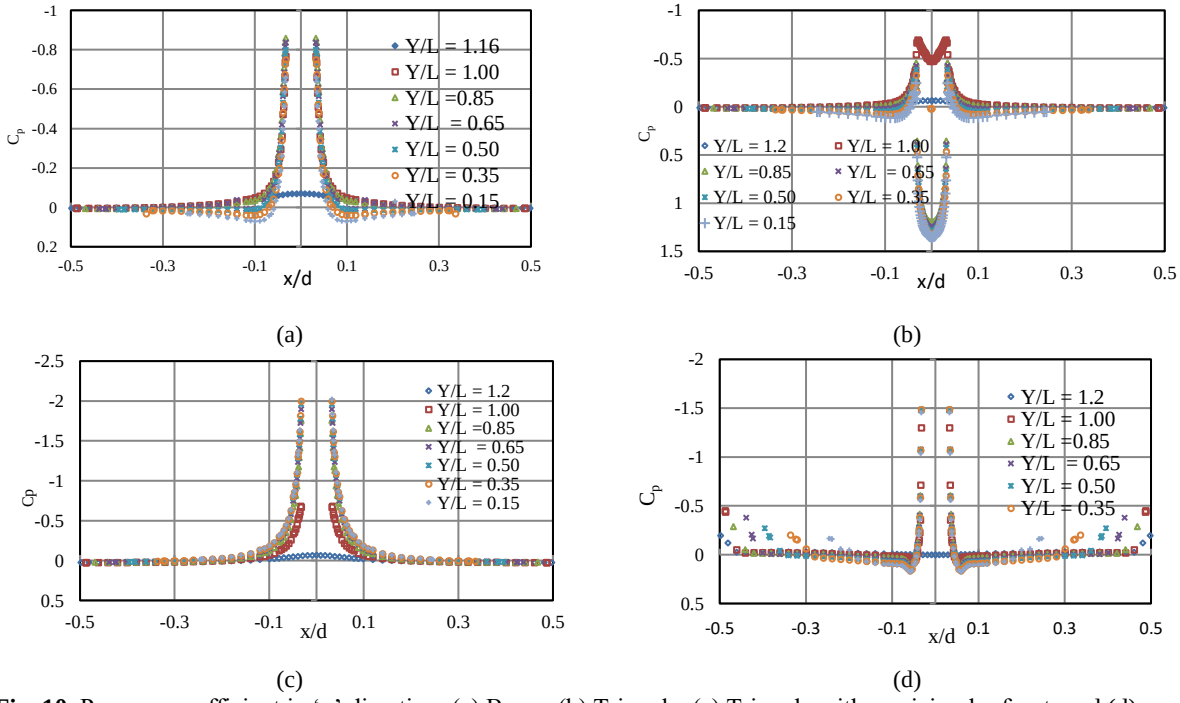

Fig. 10. Pressure coefficient in 'x' direction: (a) Beam, (b) Triangle, (c) Triangle with semicircular front, and (d) Cylinder.

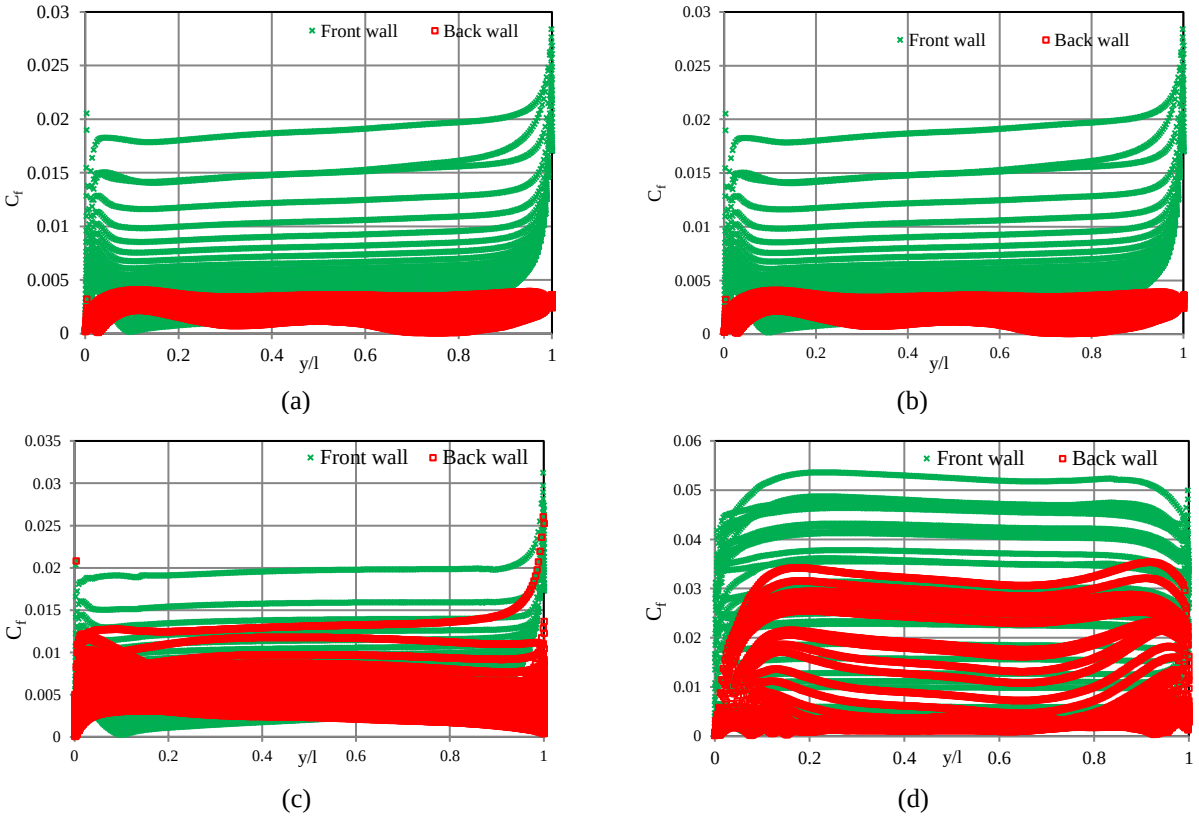

Fig. 11. Wall friction coefficient: (a) Beam, (b) Triangle, (c) Triangle with semicircular front, and (d) Cylinder

Compared to pressure coefficient, frictional coefficient at beam and triangle is negligible and is in the range of 1% to 2% of pressure coefficient. For cylinder it is in the range of 2% to 3%. It is in line with the value of up to 3% reported by Achenbach [26]. Hence, for a drag coefficient estimate, the effect of frictional forces is negligible and it can be eliminated.

6.4. Velocity distribution

Pressure force is a combination of pressure due to static pressure and dynamic pressure. In dynamic force estimation, the velocity of the fluid acting on the body plays a major role. So velocity distribution in the flow domain is discussed in this section. Velocity distribution contours for a sample case, having beam as a bluff body at a reference Reynolds number is as shown in Fig. 12. From the velocity contour, it is observed that the maximum velocity ratio of 1.3 times is near the tip of the beam. Due to blockage of the beam in the flow, recirculation is formed and flow is moving towards the back side wall; and it reduces the velocity ratio up to 0.47. It leads to producing an additional dynamic force on the back wall.

For plotting the results in axial and radial directions of the flow, Line/rack are considered and are as given in Fig. 7. For better representation, ratio between the instantaneous and inlet velocity is plotted.

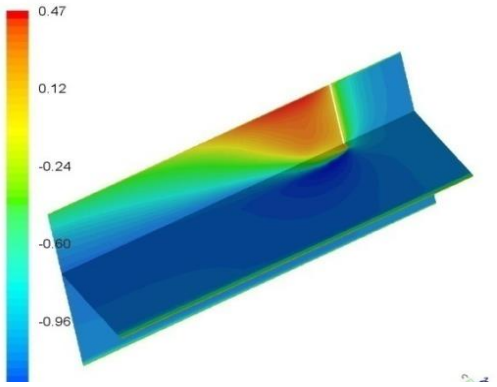

Fig. 12. Velocity distribution contour.

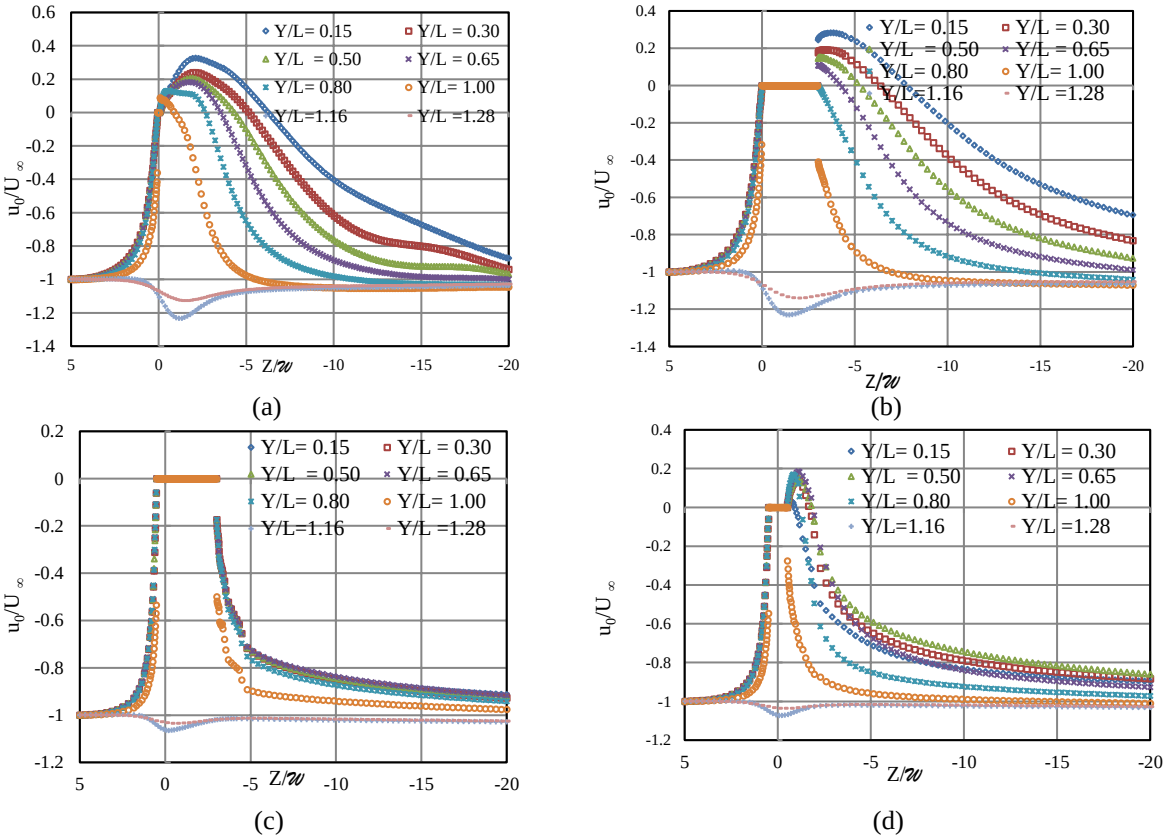

Fig. 13. Axial velocity (plotting plane XZ): (a) Beam, (b) Triangle, (c) Triangle with semicircular front, and (d) Cylinder.

The axial velocity ratio in axial direction is as given in Fig. 13. The inlet side velocity ratio is constant up to the 2.5 times of 'z/w' ratio.

From that location, it exponentially reduces and reaches the value of zero at the front wall. Near the back wall, the flow is in the reverse direction and it will produce a dynamic force on the back wall. It is true for all cases, except the triangle with semicircular front. There is no reverse flow in this case.

Radial velocity in XZ plane is plotted and is as shown in Fig. 14. When the flow is approaching the front wall, due to obstruction of flow in the axial direction, velocity in that direction will reach to zero. Since the flow cannot be stopped, its direction has been changed from axial to radial with a velocity ratio of 1.0 at front wall. It has been observed in all four cases. In the downstream side of the bluff body, flow velocity has been fully changing its direction from radial to axial. In the case of the beam it is happening at 'z/w' ratio of 20, 7 for cylinder and 5 for a triangle with circular front. In triangular bluff body, velocity ratio was reducing to 0.2 time at 'z/w' ratio of 20.

Axial and radial velocity in the 'XY' plane, which coincides with the Centre line of bluff body is plotted and given in Fig. 15. and Fig. 16. respectively. Due to the geometrical similarity of beam and triangle, in the plane where the results are compared, there isa similar trend in its axial velocity. The velocity ratio slightly increases from 1.00 to 1.10 and it is due to the blockage effect of bluff body. In the case of a cylinder and triangle with semicircular front,there are similar trends with an increase in velocity ratio of 1.00 to 1.5. For all cases when approaching near the pipe wall, the axial velocity ratio is reducing to zero.

From the plots of radial velocity in 'XY' plane, it is observed that both beam and triangle have similar patterns with a maximum radial velocity ratio of 0.6 and is near the side walls of bluff body.

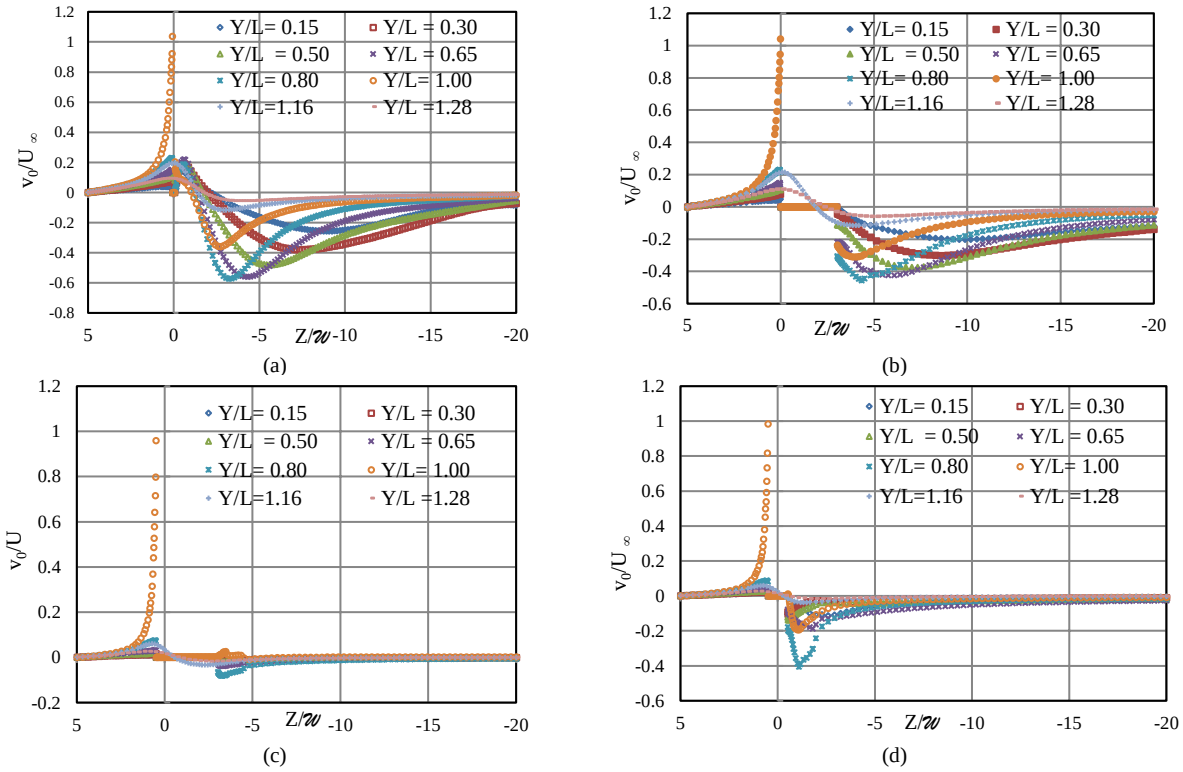

Fig. 14. Radial velocity (plotting plane XZ): (a) Beam, (b) Triangle, (c) Triangle with semicircular front, and (d) Cylinder.

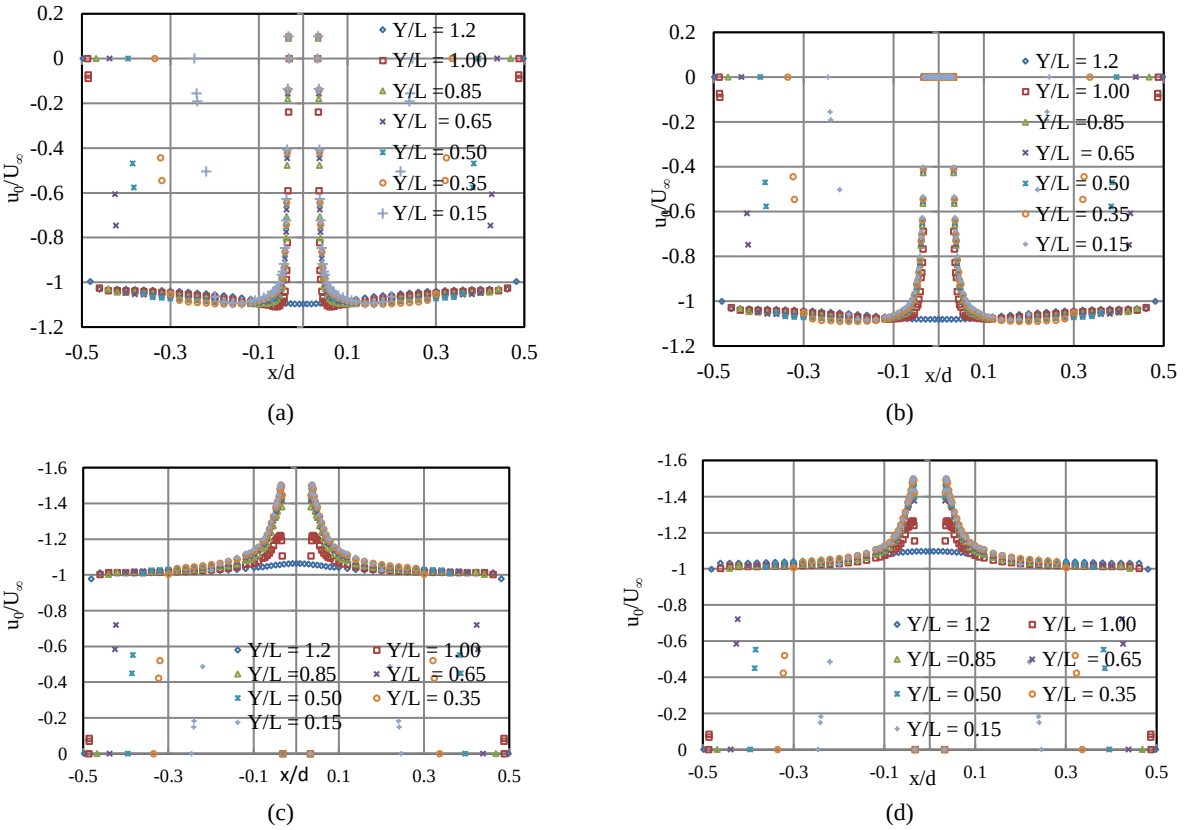

Fig. 15. Axial velocity (plotting plane XY): (a) Beam, (b) Triangle, (c) Triangle with semicircular front, and (d) Cylinder.

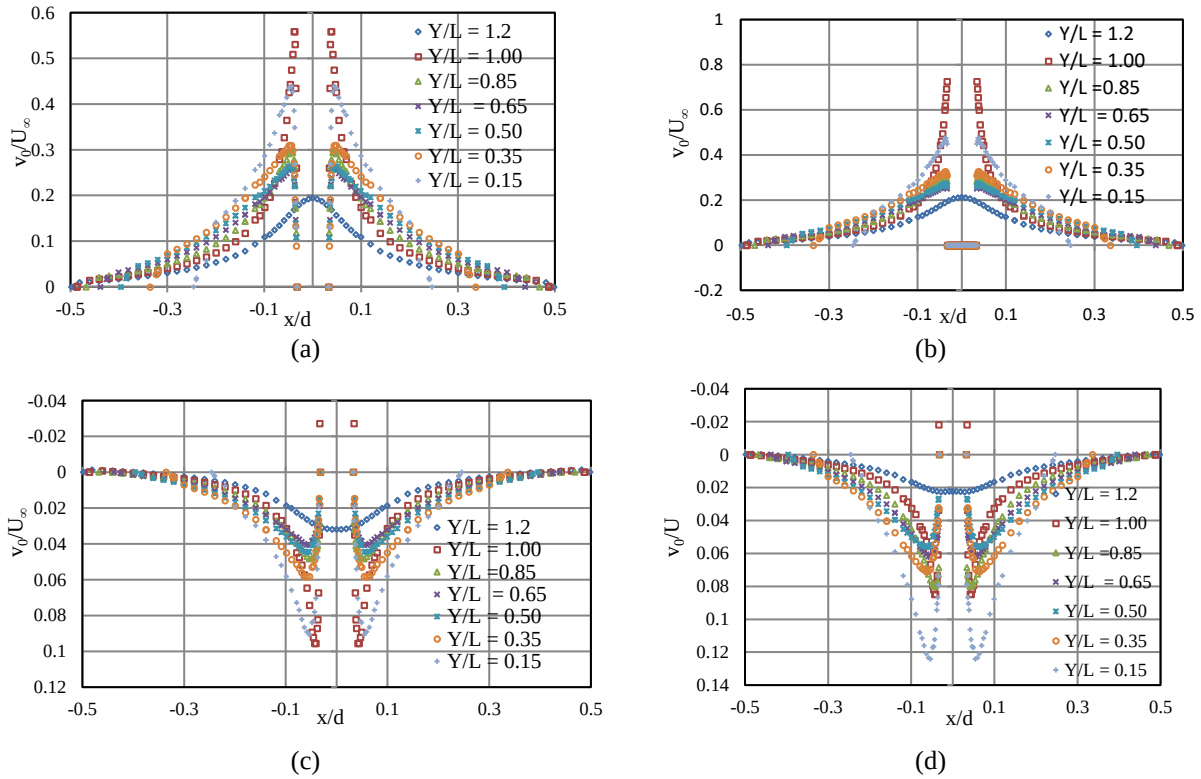

Fig. 16. Radial velocity (plotting plane XY): (a) Beam, (b) Triangle, (c) Triangle with semicircular front, and (d) Cylinder.

When the plotting plane is away from the bluff body, the velocity ratio is approaching to 0.2, which is near the tip of the body and is due to the reduced in flow area in that plane. For cylinder and semicircular front to a triangle, a similar trend has been observed with a maximum velocity ratio of 0.1.

From the plots of radial velocity in 'XY' plane, it is observed that both beam and triangle have similar patterns with a maximum radial velocity ratio of 0.6 and is near the side walls of bluff body.

7. Conclusions

Three - dimensional drag coefficient of various geometrical shapes was carried out using standard k-ε model. It was done for the 'l/d' ratio of 0.1 to 1.0 for the Reynolds number range of $1.0x10^3$ to $3.6x10^5$. The hydrodynamic characteristics such as dynamic drag coefficient, pressure coefficient and friction coefficient were studied and are in line with the results reported by various researchers.

Compared with the frictional component, pressure contributes more on the total drag force acting on the bluff body. The effect of frictional force on drag force is less than 2% for beam and triangle. For other geometries studied, it is less than 3. The geometry of the bluff body has a significant effect drag coefficient. Pressure coefficient at the front side of the bluff body is playing a major role in its pressure drag. The effect of Reynolds number on drag coefficient is negligible in the range of Reynolds number studied. Irrespective to the geometry, 'l/d' ratio plays a major role in drag coefficient. For 'l/d' ratio having less than 0.2 and when it is near to 1.00, the drag coefficient has reduced drastically. Thickness effect on the beam is significant and is reduced, when the ratio reaches 1.00.

Acknowledgement

The authors wish to express gratitude to U.Muthu Kumar, SRE for providing necessary support in computational facility.

Reference

[1] W. H. Hucho, *Aerodynamics of Road Vehicles: From Fluid Mechanics to Vehicle Engineering*, 1st ed, Butterworth - Heinemann Ltd, (1987).

[2] B. E. Launder and D. B. Spalding, "The numerical computation of turbulent flows", *J. Comput. Methods Appl. Mech. Eng.*, Vol. 3, No. 2, pp. 269-289, (1974).

[3] R. D Belvins, *Applied Fluid Dynamics Handbook*, (1984), Van Noistrand reinhand company Newyark. ISBN-13: 978-1575241821.

[4] C. Norberg, "Fluctuating lift on a circular cylinder: review and new measurements", *J. Fluids Struct.*, Vol. 17, No. 1, pp. 57-96, (2003).

[5] F. Gu, J. S. Wang, X. Q. Qiao and Z. Huang, "Pressure distribution, fluctuating forces and vortex shedding behavior of circular cylinder with rotatable splitter plates", *J. Fluids Struct.*, Vol. 28, pp. 263-278, (2012).

[6] B. Zhou, X. Wang, W. M. Gho and S. K. Tan, "Force and flow characteristics of a circular cylinder with uniform surface roughness at subcritical Reynolds numbers", *Appl. Ocean Res.*, Vol. 49, pp. 20-26, (2015).

[7] B. Zhou, X. Wang, W. Guo, J. Zheng and S. K. Tan, "Experimental measurements of the drag force and the near-wake flow patterns of a longitudinally grooved cylinder", *J. Wind Eng. Ind. Aerodyn.*, Vol. 145, pp. 30–41, (2015).

[8] I. P. Castro, "Wake characteristics of two – dimensional perforated plates normal to an air-stream", *J. Fluid Mech.*, Vol. 46, No. 3, pp. 599-609, (1971).

[9] Lisoski and D. L. Ashton "*Nominally two-dimensional flow about a normal flat plate*", Ph.D. Thesis, California Institute of Technology, (1993).

[10] B. Rostane, A. Khaled and S. Abboudi, "Influence of insertion of holes in the middle of obstacles on the flow around a surface-mounted cube", *J. Comput. Appl. Res. Mech. Eng.*, Vol. 9, No. 1, pp. 77-87, (2019).

[11] A. Khalkhali and H. Safikhani, "Applying evolutionary optimization on the airfoil design*", J. Comput. Appl. Res. Mech. Eng.*, Vol. 2, No. 1, pp. 51-62, (2012).

[12] F. M. Najjar and S. P. Vanka, "Effects of intrinsic three-dimensionality on the drag characteristics of a normal flat plate", *Phys. Fluids*, Vol. 7, pp. 2516–2518, (1995).

[13] A. Fage and F. C. Johansen, "On the flow of air behind an inclined flat plate of infinite span, "*Proc. R. Soc. Lond.*". Series A, Vol. 116, No. 773, pp. 170-197, (1927).

[14] P. Dey and A. Kr. Das, "Numerical analysis of drag and lift reduction of square cylinder", *Int. J. Eng. Sci. Technol.*, Vol.18, No. 4, pp. 758-768, (2015).

[15] A. M. Bimbato, L. A. A. Pereira and M. H. Hirata, "Simulation of viscous flow around a circular cylinder near a moving ground", *J. Braz. Soc. Mech. Sci. Eng.*, Vol. 31, No. 3, pp. 243-252 (2009).

[16] K. Karthik, M. Vishnu, S. Vengadesan and S. K. Bhattacharyya, "Optimization of bluff bodies for aerodynamic drag and sound reduction using CFD analysis", *J. Wind Eng. Ind. Aerodyn.*, Vol. 174, pp. 133-140, (2018).

[17] X. Tian, M. C. Ong, J. Yang and D. Myrhaug, "Large-eddy simulation of the flow normal to a flat plate including corner effects at a high Reynolds number", *J. Fluids Struct.*, Vol. 49, pp. 149-169, (2014).

[18] S. Chakraborthy, "Course note on Introduction to turbulence modeling module No 1", *IIT, Kharagpur*.

[19] F. H Harlow and P. I. Nakayama, "Transport of turbulence energy decay rate", *Los Alamos Sci. Lab., University California Report LA-3854*, (1968).

[20] B. Launder, A. Morse, W. Rodi and D. B. Spaldiug, "The prediction of free shear flows - A comparison of the performance of six turbulence models", *Proc. of NASA Conf. on Free Shear Flows*, Langley (1972). Corpus ID: 118099033.

[21] N. Koutsourakis, J. G. Bartzis and N. C. Markatos, "Evaluation of Reynolds stress, k-ε and RNG k-ε turbulence models in

street canyon flows using various experimental datasets", *Environ. Fluid Mech.*, Vol. 12, No. 4, pp. 379–403, (2012).
[22] *ANSYS Meshing User's Guide Release* 15.0, (2013).
[23] F. M. Najjar and S. Balachandar, "Low-frequency unsteadiness in the wake of a normal flat plate", *J. Fluid Mech.*, Vol 370, pp. 101–147, (1998).
[24] V. D. Narasimhamurthy and H. I. Andersson, "Numerical simulation of the turbulent wake behind a normal flat plate", *Int. J. Heat Fluid Flow*, Vol. 30, No. 6, pp. 1037-1043, (2009).
[25] B. R. Munson, A. P. Rothmayer, T. H. Okiishi and W. W. Huebsch, "*Fundamentals of Fluid Mechanics*", 16th edition, "John Wiley and Sons, Inc, (2009) ISBN-13:978-1118116135.
[26] E. Achenbach, "Distribution of local pressure and skin friction around a circular cylinder in cross-flow up to Re 5e+6", *J. Fluid Mech.*, Vol. 34, No. 4, pp. 625–639, (1968).

How to cite this paper:

A. Tamil Chandran, T. Suthakar, K. R. Balasubramanian, S. Rammohan and Jacob Chandapillai, "Numerical prediction of the drag coefficient of bluff bodies in three-dimensional pipe flow,", *J. Comput. Appl. Res. Mech. Eng.*, Vol. 12, No. 1, pp. 13-29, (2022).

DOI: 10.22061/JCARME.2021.7114.1931

URL: https://jcarme.sru.ac.ir/?_action=showPDF&article=1622